Proceedings of the ASME 2024 19th International Manufacturing Science and Engineering Conference
MSEC2024
June 17-21, 2024, Knoxville, Tennessee

MSEC2024-123865

BRIEF PAPER: DECIPHERING THE EFFECT OF PART THERMAL HISTORY ON MICROSTRUCTURE AND MECHANICAL PROPERTIES IN LASER POWDER BED FUSION OF SS316L

Kaustubh Deshmukh
Virginia Tech
Blacksburg, VA

Alex Riensche
Virginia Tech
Blacksburg, VA

Ryan J. Lane
Virginia Tech
Blacksburg, VA

Kyle Snyder
CCAM
Disputanta, VA

Christopher B. Williams
Virginia Tech
Blacksburg, VA

Reza Mirzaeifar
Virginia Tech
Blacksburg, VA

Prahalada Rao
Virginia Tech
Blacksburg, VA

ABSTRACT

The main research goal of this study is to decipher the intercorrelation between process-induced thermal-structure-property relationships of Stainless Steel 316L fabricated by laser powder bed fusion. The objective therein is achieved by explaining and quantifying the effect of processing parameters and part-scale thermal history on microstructure evolution and mechanical properties of these parts. Multiple previous works have correlated the effect of process parameters on flaw formation, microstructural features evolved and functional properties; however, a lack of understanding remains in the underlying effect of the thermal history on part microstructure and mechanical properties. The thermal distribution, or thermal history, of the part as it is being built layer-by-layer is influenced by the processing parameters, material properties and shape of the part. The thermal history influences the microstructure by changing the grain structure evolution, which affects the part properties. Therefore, the novelty of this paper lies in illuminating the process-thermal history-microstructure-property relationship in laser powder bed fusion.

Characterization of tensile specimens processed at a variety of conditions reveal a direct influence of the choice of process parameters on the dendritic structure and the grain orientations. A high energy density leads to <100> textured columnar dendritic grains and low energy density leads to randomly oriented equiaxed grains as a result of the shifting heat influx. The tensile properties are correlated with the inherent microstructure. Through future work involving fracture surface analysis, the texture, grain size and porosity is expected to influence the inherent fracture mechanism.

This work demonstrates that an understanding of thermal distribution within a printed part can inform the choice of processing conditions to generate the final microstructure as per the specified functional requirements. Thus, this paper lays the foundation for future prediction and control of microstructure and functional properties in laser powder bed fusion by identifying the root fundamental thermal phenomena that influences the microstructure evolution and part properties.

Keywords: Metal Additive Manufacturing, Laser Powder Bed Fusion, Microstructure, Thermal Modeling, Tensile Testing.

1. INTRODUCTION

Laser powder bed fusion (L-PBF) is an additive manufacturing (AM) process in which metal powders are raked or rolled over a build plate, and selectively melted by a high energy input laser source [1, 2]. However, this advancement in metal AM comes at the cost of introducing defects such as lack of fusion voids, porosities (through gas entrapment and interlayer), keyholes and inclusions in L-PBF. The presence of such defects can adversely affect the mechanical performance of printed parts [3, 4]. The localized melting of metal powders in L-PBF results in high thermal gradients and unidirectional heat flow across the build layers that results in a complex hierarchical and anisotropic solidification structure. Such a microstructure leads to anisotropic functional properties which makes it difficult to standardize parts made by L-PBF [5-7].

The choice of process parameters (e.g., laser power, scan speed, hatch spacing, etc.) influences the meltpool scale as well as part-scale thermal profile and thereby increases the complexity in understanding the microstructure of the printed parts. The part thermal history is also influenced by the material properties, shape of the part and location on the build plate [8]. The thermal history influences the growth kinetics governing microstructure evolution which in turn affects the part properties [9]. Such a process-thermal-structure-property relationship underscores the criticality of understanding the layer-by-layer

spatio-temporal thermal distribution as a function of the processing conditions, and subsequently, predict its effect on the underlying microstructure to better predict the performance of final parts [10].

The overall aim of this work is to present a framework in which process-induced thermal history is correlated to the characterized microstructure and the final part properties. Part thermal distributions are simulated using a rapid, meshless, graph-theory derived thermal modeling approach developed in our previous works [3, 11-13]. This model is then used to gain an understanding on the evolution of grain shape, morphology, structure, size and texture and the tensile performance. This approach is summarized in Figure 1.

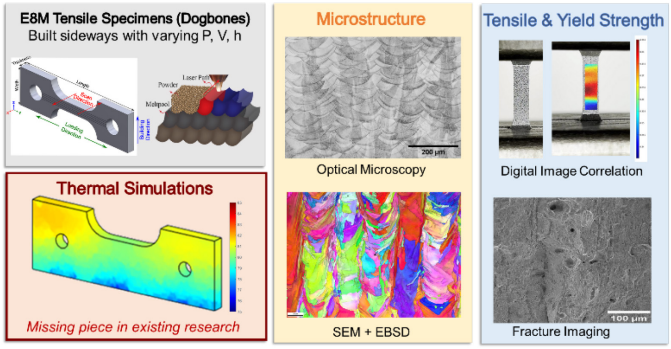

Figure 1: SUMMARY OF THE TEST PLAN USED IN THIS RESEARCH STUDY.

2. MATERIALS AND METHODS

2.1 Experimental Setup

L-PBF parts were made using an EOS M290 machine with SS 316L powders, facilitated by the Commonwealth Center for Advanced Manufacturing (CCAM). 40 parts shaped like tensile dog bones were made on a single build plate, as shown in FIGURE 2a. The final tensile specimens were cut from the printed parts by EDM. The as-printed parts have dimensions as shown in FIGURE 2b; the final dog bone dimensions after EDM are shown in the black inset. The four processing conditions used in this study and resultant volumetric energy densities are given in Table 1. Nominal process parameters used for S2 were based on the manufacturer recommended settings for SS316L. The build plate was preheated to 70 °C. A layer height of 20 µm and a laser spot size of 70 µm were fixed, and a bi-directional scan strategy was used for all the four sets.

TABLE 1: PROCESSING PARAMETERS USED IN THIS STUDY TO FABRICATE FOUR SETS S1 TO S4 WITH S2 BEING THE MANUFACTURER RECOMMENDED CONDITION.

Set	Laser Power (P) [W]	Scan Velocity (V) [mm/s]	Hatch Spacing (H) [µm]	Energy Density $=\frac{P}{V \cdot H \cdot L}$ [J·mm^{-3}]
S1	225	1000	90	125
S2	195	1083	90	100
S3	150	1100	75	90
S4	175	1200	100	73

The process parameters are varied in such a way that the resultant sets are expected to have a variable meltpool size. Meltpool size and shape has been shown to be a direct outcome of the thermal distribution and influences the grain structure [8]. In addition, with higher energy density and laser power, keyhole porosities may be induced whereas, with lower energy densities and laser power, lack of fusion voids may be induced [11].

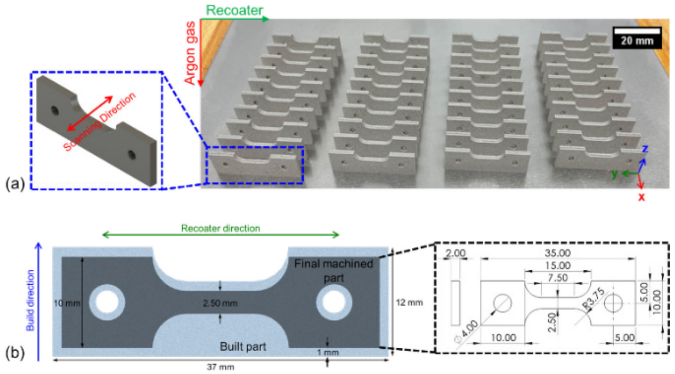

FIGURE 2: (a) A PICTURE OF THE BUILD PLATE SHOWING 40 SS316L PARTS PRINTED VIA L-PBF (CAD MODEL IN BLUE INSET). (b) FINAL PRINTED PARTS FROM WHICH THE TENSILE DOG BONES ARE RETRIVED BY EDM (FINAL DIMENSIONS IN THE BLACK INSET).

2.2 Characterization

Samples (one each from the four sets) were prepared by grinding and polishing. The microstructure characterization was first done through scanning electron microscopy (SEM) and optical microscopy. Subsequently, electron back scatter diffraction (EBSD) measurements were performed using an EDAX Hikari detector. The data processing for the same was done through TSL OIM software from EDAX. Optical, SEM and EBSD measurements were all performed in the gauge section of the final dog bones. Further, 3 samples per set were tensile tested to generate the stress-strain data for these dog bones.

2.3 Graph theory thermal model

The temperature distribution and cooling rate in L-PBF is influenced by the part shape, material properties, and processing parameters. The part thermal history in turn impacts the microstructure evolved. Typically, obtaining the part-scale thermal distribution involves solving the heat diffusion equation, Eqn. (1) using the finite element (FE) method.

$$\overbrace{\widehat{\rho c_p}}^{\substack{Material\\Properties}} \frac{\partial T(x,y,z,t)}{\partial t} - k\overbrace{\left(\frac{\partial^2}{\partial x^2}+\frac{\partial^2}{\partial y^2}+\frac{\partial^2}{\partial z^2}\right)}^{Shape\ of\ the\ Part}\overbrace{T(x,y,z,t)}^{\substack{Part\\Temperature}} = Q \qquad (1)$$

In this equation, T at a location (x, y, z) is the solution at time t. Serving as the material constants, ρ is the material density [kg·m^{-3}], c_p is the specific heat [J·kg^{-1} ·K^{-1}], and k is the conductivity [J·s^{-1} ·m^{-1}·K^{-1}]. Q is the heat input per second of the material melted per unit volume [J·s^{-1}·m^{-3}].

However, solving this equation with FE is computationally expensive and time consuming. To overcome this, our previous works have established a mesh-free thermal model based on

graph theory. [3, 12, 13] Solving Eqn. (1) by graph theory yields a semi analytical solution in the form of Eqn. (2).

$$T(x,y,z,t) = \phi e^{-\frac{k}{\rho c_p}\Lambda t}\phi'\left(\frac{A_e S_l}{\rho v c_p}\frac{P}{V} + T_{prev}\right) \quad (2)$$

The eigenvalues (Λ) and eigenvectors (ϕ) at time t are constructed on a discrete set of nodes representing the geometry of the part. A_e is the effective laser absorptivity, S_l length scanned per layer [mm], P laser power [W], V laser velocity [mm·s-1], v volume of material melted in a layer [mm^3], and T_{prev} temperature of the previous layer (from simulation, [°C]). This equation can be used to rapidly estimate sub-surface end of cycle temperature (T_e) and cooling time (t_c).

This graph theory model also incorporates boundary conditions defined by the heat losses to the build chamber, the surrounding powder and to the build plate i.e., substrate. To identify these boundary conditions, model calibrations on the same L-PBF machine with the same material were performed in a separate work. For brevity and relevance, the model calibration results are omitted from this work.

3. RESULTS AND DISCUSSION

3.1 Microstructure characterization

SEM images of the etched microstructure of L-PBF dog bones fabricated using the four sets from TABLE 1 are shown in FIGURE 3. All four processing conditions demonstrate a familiar fish scale structure where the meltpools are visible within the build layers, a characteristic of L-PBF process. FIGURE 3a shows the SEM image of S1, where the columnar dendrites are clearly visible and seen stretching across the meltpool boundaries preferentially along the large white arrows and the building direction (red inset).

FIGURE 3d shows the SEM image of S4, where the meltpool boundaries are distinctly visible. Within the meltpools, there are clusters of grains with a cellular structure (blue inset). This cellular structure is an artifact of the randomly oriented dendrites. FIGURE 3b shows the micrograph of S2 where, in addition to the columnar dendrites such as in S1, there are a few clusters of randomly oriented grains like in S4 (white outlines). In case of S3, the columnar dendrites are shorter than S1 and S2, and are also restricted to individual meltpool, as shown in FIGURE 3c.

When qualitatively comparing the meltpool shape and size of the four sets, S1 has the widest and deepest meltpool due to high laser power and energy density. S2 has a shallower meltpool than S1 due to reduced energy density, and S3 has a very shallow meltpool due to lower laser power. S4 has the smallest and narrowest meltpool due to faster scan speed and a lower energy density. When comparing the grain structure, columnar dendrites in S1 (seen from its optical image in FIGURE 4a) and S2 overlap multiple meltpool layers, whereas the columnar dendrites in S3, and randomly oriented cellular structure in S2 and S4 (seen from its optical image in FIGURE 4b, are constricted to an individual meltpool.

Due to the lowest laser power of 150 W used on S3, this set suffers from lack of fusion pores, as seen from the dashed white ovals in FIGURE 3c. The lower laser power is not sufficient to fuse the overlapping hatch in subsequent laser tracks, which leads to a jagged pore geometry. Future evaluation to quantify the presence of pores will be done using XCT analysis.

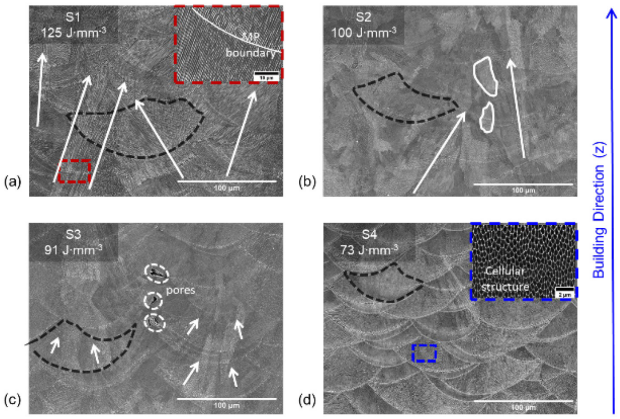

FIGURE 3: SEM IMAGES OF THE SAMPLE SETS S1 TO S4 FABRICATED BY L-PBF. MELTPOOL BOUNDARIES ARE VISIBLE IN ALL THE SETS RESEMBLING A FISH SCALE STRUCTURE. PROCESSING CONDITIONS AFFECT THE RESULTANT ENERGY DENSITY WHICH IN TURN CONTROL THE NATURE OF DENDRITIC GROWTH.

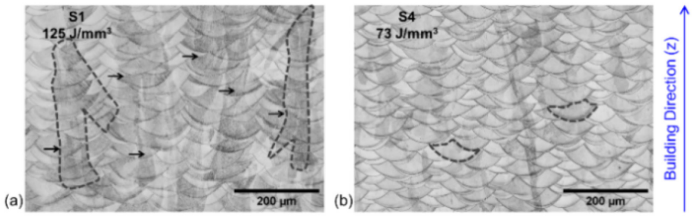

FIGURE 4: OPTICAL MICROSCOPY IMAGES FOR SAMPLE SETS (a) S1 SHOWING THE COLUMNAR DENDRITIC GROWTH ACROSS MULTIPLE MELT POOL LAYERS / BOUNDARIES AND (b) S2 SHOWING THE CELLULAR STRUCTURE RESTRICTED TO THE INDIVIDUAL MELT POOLS.

3.2 Electron backscatter diffraction (EBSD)

The orientation maps and inverse pole figures (IPF) along the building direction of the dog bones are generated from EBSD measurements. EBSD orientation map of S1 shown in FIGURE 5a1 sheds further light on the overlapping columnar grain structure. A high laser power and resultant high heat input remelts the previously solidified layer leading to epitaxial grain growth and grain coarsening. S1 has an average grain size of 37.6 µm and 17.5 % grains larger than 50 µm, as seen from FIGURE 6a. A strong <100> texture is observed along the building direction as seen from FIGURE 5a2.

A decrease in laser power and a faster scan speed reduces the energy density which in turn curtails the excessive remelting in the case of S2. Therefore, the grain structure of S2 as seen in FIGURE 5b1 consists of a mixture of coarsened columnar grains and an equiaxed grain structure. This is evident from the average grain size of 24.3 µm and 12.5 % grains larger than 50 µm as seen from FIGURE 6b. Due to low laser power and energy density in S3 and S4, the average grains size drops to 18.4 and

20.6 µm respectively. Both the sets have nearly 94 % grains smaller than 50 µm.

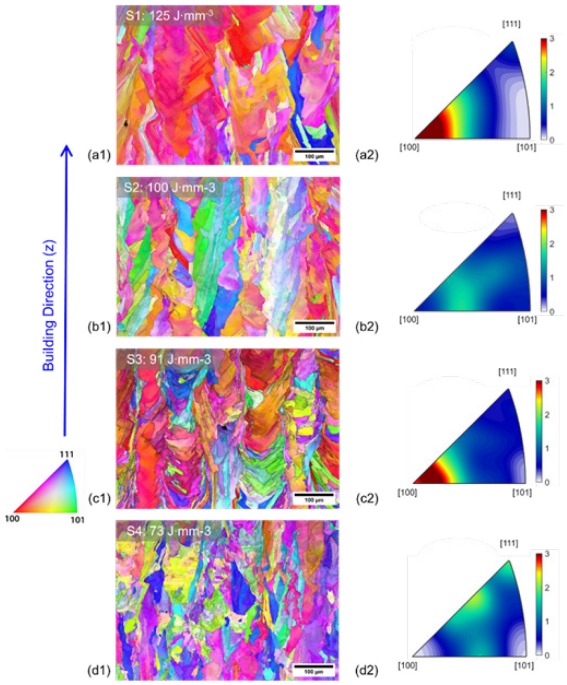

FIGURE 5: (A1-D1) ORIENTATION MAPS AND (A2-D2) INVERSE POLE FIGURES (IPF) ALONG THE BUILDING DIRECTION IN SAMPLE SETS (A1, A2) S1, (A2, D2) S2, (A3, D3) S3 AND (A4, D4) S4. THE GRAIN MORPHOLOGY, SIZE AND TEXTURE IS SEEN TO BE VARYING ACROSS THE FOUR SETS AS A FUNCTION OF THE PROCESSING PARAMETERS.

Due to the presence of randomly oriented grains of equiaxed nature, S2 and S4 do not display any preferred texture along the building direction as seen from FIGURE 5b2 and FIGURE 5d2. The grain structure of S3 is distinct with horizontal chevron patterns formed as a result of the lath-like fine columnar grains that are restricted within the individual meltpool. Despite being smaller than in S1, these columnar grains are still seen to be preferentially growing along <100> in the building direction as seen in FIGURE 5c2.

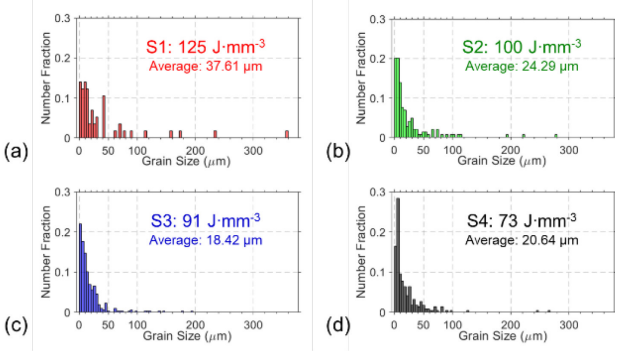

FIGURE 6: GRAIN SIZE DISTRIBUTION OF THE SAMPLE SETS S1 TO S4 OBTAINED FROM EBSD MEASUREMENTS PERFORMED ON THE L-PBF PARTS. GRAIN SIZE VARIES AS A FUNCTION OF LASER POWER AND HEAT INPUT.

3.3 Mechanical behavior

Representative tensile curves of the tensile tests of the four parameter sets S1-S4 are reported in FIGURE 7a. From FIGURE 7b, the yield stress and tensile stress of S1 and S2 show a considerable overlap even though their microstructures vary. However, the yield and tensile stress of S3 and S4 are seen to be reduced compared to S1 and S2 even though they have a finer grain size. This shows that there are other factors at play that negate the Hall-Petch relationship in these cases. Especially in case of S3, the preliminary microstructure results display that this set has lack of fusion pores which have been proven to be detrimental for tensile strength of L-PBF parts [6]. Similarly, S4 has the lowest strength. The low energy density in S4 is likely to induce microstructural features that are not distinguishable from the current characterization steps. This behavior could be explained through fracture surface analysis as part of our future work.

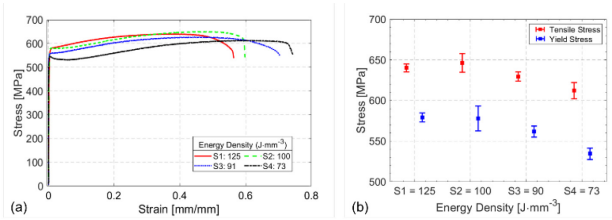

FIGURE 7: (a) TENSILE CURVES OBTAINED FROM THE DIC TESTS AND (b) YIELD AND TENSILE STRESS DATA OBTAINED FROM THE TENSILE CURVES. S1 AND S2 HAVE SIMILAR TENSILE PERFORMANCE WHEREAS S3 AND S4 HAVE A REDUCED STRENGTHS COMPARED TO S1 AND S2, WITH S4 HAVING THE LEAST STRENGTH.

3.4 Graph theory thermal modeling

In a single layer wise cycle, the laser strike at a specific spot heats up the SS316L powders above its melting point. As the laser spot moves to subsequent scanning regions, the melted powders left in its track cool down and rapidly solidify. This solidification occurs through heat losses to the build chamber, powder bed, and the build plate. Of these, conductive heat losses to the build plate are most dominant [13]. Therefore, the heat flows from the melted volume at the top surface towards the build plate which leads to a preferential solidification in the opposite path along the building direction.

A high laser power and energy density in S1 and S2 leads to a steep thermal gradient along the building direction and a large meltpool volume, as seen from the results in FIGURE 8. Steep thermal gradients cause the heat flow to take place from the solidifying layer to the solidified layers beneath, and subsequently into the build plate. This promotes the grain growth to take place along building direction leading to the coarse and textured microstructure observed in S1 (FIGURE 5a1). Similarly, a reduced energy density in S3 and S4 leads to reduced thermal gradients than in S1. Due to a lower heat input, a lower volume of material is melted beneath the top powder surface, reducing the thermal gradients. This leads to a randomly oriented grain texture as seen in FIGURE 5b2 and FIGURE 5d2.

End-of-cycle temperature (T_e) is analogous to the average surface temperature of a melted layer after a new powder layer is deposited on top, but just before melting of the next layer is initiated by the laser. A higher volume of material melted in higher energy density sets leads to a higher heat buildup. From S4 to S1, in the same timeframe of a specific layer height being built, this increases the temperature up to which a layer cools down.

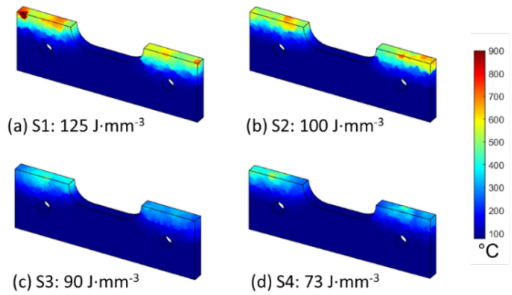

FIGURE 8: RESULTS OF THE SIMULATED THERMAL GRADIENTS IN ALL THE FOUR PROCESSING CONDITIONS AT A TIME STEP OF 0.5 S AFTER THE LASER STRIKE AT THE TOP SURFACE IN 600th LAYER.

FIGURE 9b shows the average layer wise cooling times (t_c) for all the four sets used in this study. Results show that S1 has the highest t_c. This means S1 takes the longest time to cool down from 1600°C to 700°C. Thus, it can also be considered that S1 has lowest cooling rate of the four sets in this temperature range. With decreasing energy density, t_c decreases. This is because a lower melted volume from a reduced heat input will cool down and solidify faster. A higher cooling rate in turn leads to a finer grain structure as seen in FIGURE 6 for S3 and S4.

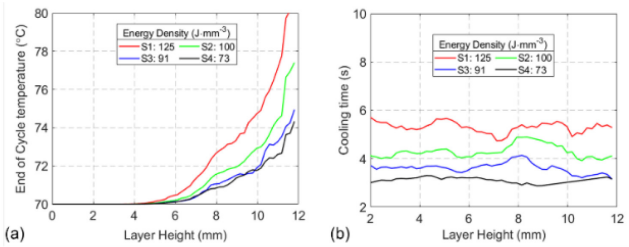

FIGURE 9: (a) SUBSURFACE END-OF-CYCLE TEMPERATURE – T_e AND (b) COOLING TIME – t_c, FROM 1600 °C TO 700 °C FOR EVERY NEW LAYER DEPOSITED, PREDICTED FROM THE GRAPH THEORY THERMAL MODEL.

4. CONCLUSIONS

The thermal history influences the microstructure evolution, which affects the part properties. For each processing condition, the spatial temperature gradients and sub-surface cooling rates are generated from a physics-based computational thermal model and correlated with the characterized microstructure. With decreasing energy density, the thermal gradients decrease while the cooling rates increase; both leading to a gradual shift from textured columnar grains to randomly oriented equiaxed grains. Therefore, the novelty of this work lies in creating a computational-experimental framework for illuminating the process-thermal history-microstructure-property relationship in L-PBF. This framework serves as a precursor for the future objective of predicting the microstructure and mechanical properties as a function of the processing parameters.

REFERENCES

1. DebRoy, T., et al., *Additive manufacturing of metallic components – Process, structure and properties.* Progress in Materials Science, 2018. **92**: p. 112-224.
2. Vafadar, A., et al., *Advances in Metal Additive Manufacturing: A Review of Common Processes, Industrial Applications, and Current Challenges.* Applied Sciences, 2021. **11**(3): p. 1213.
3. Riensche, A., et al., *Feedforward control of thermal history in laser powder bed fusion: Toward physics-based optimization of processing parameters.* Materials & Design, 2022. **224**.
4. Chowdhury, S., et al., *Laser powder bed fusion: a state-of-the-art review of the technology, materials, properties & defects, and numerical modelling.* Journal of Materials Research and Technology, 2022. **20**: p. 2109-2172.
5. Ghorbanpour, S., et al., *Effect of microstructure induced anisotropy on fatigue behaviour of functionally graded Inconel 718 fabricated by additive manufacturing.* Materials Characterization, 2021. **179**.
6. Agrawal, A.K., G. Meric de Bellefon, and D. Thoma, *High-throughput experimentation for microstructural design in additively manufactured 316L stainless steel.* Materials Science and Engineering: A, 2020. **793**.
7. Popovich, V.A., et al., *Functionally graded Inconel 718 processed by additive manufacturing: Crystallographic texture, anisotropy of microstructure and mechanical properties.* Materials & Design, 2017. **114**: p. 441-449.
8. Fonda, R.W. and D.J. Rowenhorst, *Crystallographic Variability in Additive Manufacturing*, in *42nd Risø International Symposium on Materials Science*. 2022, IOP Conference Series: Materials Science and Engineering.
9. Ahmed, N., et al., *Process parameter selection and optimization of laser powder bed fusion for 316L stainless steel: A review.* Journal of Manufacturing Processes, 2022. **75**: p. 415-434.
10. Collins, P.C., et al., *Microstructural Control of Additively Manufactured Metallic Materials.* Annual Review of Materials Research, 2016. **46**(1): p. 63-91.
11. Agrawal, A.K., B. Rankouhi, and D.J. Thoma, *Predictive process mapping for laser powder bed fusion: A review of existing analytical solutions.* Current Opinion in Solid State & Materials Science, 2022. **26**.
12. Yavari, R., et al., *Part-scale thermal simulation of laser powder bed fusion using graph theory: Effect of thermal history on porosity, microstructure evolution, and recoater crash.* Materials & Design, 2021. **204**.
13. Yavari, R., et al., *Thermal modeling in metal additive manufacturing using graph theory – Application to laser powder bed fusion of a large volume impeller.* Additive Manufacturing, 2021. **41**.